Journal of Geophysical Research: Atmospheres

Supporting Information for:

Closing the reactive carbon flux budget: Observations from dual mass spectrometers over a coniferous forest

Michael P. Vermeuel[1], Dylan B. Millet[1*,] Delphine K. Farmer[2], Matson A. Pothier[2], Michael F. Link[2^], Mj Riches[2], Sara Williams[2], Lauren A. Garofalo[2]

[1] Department of Soil, Water, and Climate, University of Minnesota – Twin Cities, St. Paul, MN, USA

[2] Department of Chemistry, Colorado State University, Fort Collins, CO, USA

[^]now at Engineering Laboratory, National Institute of Standards and Technology, Gaithersburg, MD, USA

[*]Correspondence to D.B. Millet, dbm@umn.edu

Contents of this file

Text S1 to S7

Tables S1 to S5

Figures S1 to S17

Introduction

This document provides information on the following:

S1. Additional field measurement details;

S2. PTRMS laboratory calibrations and signal corrections;

S3. Flux covariance quality control;

S4. Flux spectral corrections;

S5. Modifications to land cover in the GEOS-Chem simulation;

S6. The effect of mountain-valley flow on morning MBO observations; and

S7. The assignment of rate constants to isomers and unknown species.

S1. Field collections

S1.1 Offline VOC speciation

Speciation of select VOCs emitted from ponderosa pine needles and understory species was determined using offline thermal desorption gas chromatography mass spectrometry (GC-MS) performed on sorbent tubes coupled to an online portable photosynthesis system (PPS; LI-6800, LI-COR Biosciences) (Riches et al. 2020) equipped with a 36 cm^2 needle chamber (6800-13, LI-COR Biosciences) and a large light source (6800-03, LI-COR Biosciences). Gas sampling began after plant acclimation to the PPS chamber, determined based on the stabilization of CO_2 assimilation and stomatal conductance. Two handheld pumps simultaneously pulled 4 L of air through subsampling ports up- and downstream of the PPS leaf chamber through passivated sorbent tubes packed with Tenax-TA. Tubes were analyzed offline for identification and quantification of speciated monoterpenes via thermal desorption (UNITY-xr, Markes International) and GC-MS (TRACE 1310 and ISQ, Thermo Scientific).

S1.2 HR-AMS measurements

Submicron non-refractory aerosol mass concentrations were quantified by high-resolution time-of-flight aerosol mass spectrometry (HR-AMS; Aerodyne Research Inc.) (Canagaratna et al., 2015; DeCarlo et al., 2006). The HR-AMS sampled through a ¼" OD copper inlet shared with a scanning mobility sizing spectrometer (SMPS; TSI) with a total 1.1 LPM flow rate. We operated the HR-AMS in V-mode with 5 min time resolution. The sample averaging period included 15 cycles between mass spectrometer (MS) mode (2.5s open/2.5 closed) and particle time-of-flight (PTOF) mode (15s). Organic mass is reported at ambient temperature and pressure with collection efficiency (CE) = 1. We used the ToF-AMS Analysis Toolkits v1.65B (SQUIRREL) and v1.25B (PIKA) (Aerodyne Research Inc.) in Igor Pro (Wavemetrics, Inc) for data processing. The ionization efficiency was calculated by mass comparison of 350 nm size-selected ammonium nitrate particles counted via CPC (TSI, Inc.) Relative ionization efficiencies for ammonium and sulfate were determined with ammonium sulfate and ammonium nitrate. The lower limit of detection (3× the standard deviation of in-field measurements of air collected through a HEPA filter) for OA was 0.11 $\mu g\ m^{-3}$.

S1.3 PTRMS sampling conditions

The PTRMS inlet was teed into a 1.0 m bypass (composed of 1/8" ID PFA tubing) that subsampled from the sampling manifold at 4000 standard cubic centimeters per minute (sccm). Bypass pressure was held at 660 mbar, allowing the instrument drift tube to draw an 80 sccm mass flow, and a supplemental bypass was used to draw an additional 150 sccm through the heated (80°C) 1.5 m, 1/16" ID PFA PTRMS inlet. An inline 47 mm diameter, 5 μm pore-size filter was installed within the sampling bypass, with routine replacements approximately every three days.

S1.4 ICIMS – In-field voltage scanning (dV_{50}) and laboratory calibrations to determine bulk sensitivity

While permeation tubes provided the sensitivity for select organic acids for the I^-CIMS, we determined the sensitivity for other measured ions using voltage scanning. On the evening of 22 August , we systematically changed internal voltage settings within the ion focusing region of the atmospheric pressure interface of the I^-CIMS to create a voltage differential (dV) between the "Q2-Front" and "Skimmer". During the voltage scan, we maintain the voltage differential downstream of the "Skimmer". The resulting decline of analyte signal was then subjected to an optimized sigmoidal fit algorithm to determine the representative dV_{50} value of each analyte ion (dV_{50} = inflection point in sigmoidal curve). The dV_{50} value correlates with the binding strength between I^- and the analyte molecules to form ion-molecule clusters. These dV_{50} values can thus be used to estimate sensitivities of analytes for which there are no standards (Bi et al., 2021; Iyer et al., 2016).

Following the FluCS campaign, we conducted a series of laboratory experiments to quantify the relationship between log(sensitivity) and dV_{50} (**Fig. S5**). We use this relationship to estimate the sensitivities of analyte ions measured in-field using the dV_{50} calculated for each ion. Sensitivities of calibrant compounds were determined in two ways: 1) standard addition experiments using permeation tubes of C_1-C_5 alkanoic acids; and 2) triplicate liquid injections using a Filter Inlet for Gases and AEROsols (FIGAERO) of tropic ($C_9H_{10}O_3$), myristic ($C_{14}H_{28}O_2$), and palmitic ($C_{16}H_{32}O_2$) organic acids (Lopez-Hilfiker et al., 2014). We determine the dV_{50} values of the above eight calibrants in an identical manner as the in-field voltage scanning experiments.

For determination of I^-CIMS sensitivities in the field, species that could not be fit via voltage scanning experiments or had dV_{50} values lower than 2 V and higher than 9 V were assigned the

median sensitivity value of 4.9 ncps ppt^{-1}. Species that had sensitivities higher than the collision-limit sensitivities as determined for this instrument (50 ncps ppt^{-1}) were assigned the collision-limit sensitivity (Mattila et al., 2020).

S2. Laboratory calibrations and data corrections

S2.1 Liquid calibrations

Liquid calibrations were performed for MT isomers ($C_{10}H_{16}$: α-pinene, β-pinene, limonene, ocimene), monoterpenoids ($C_{10}H_{16}O$: camphor, α-pinene oxide; $C_{10}H_{14}O$: carvone, myrtenal, perillaldehyde, verbenone) and a sesquiterpene oxide (caryophyllene oxide: $C_{15}H_{24}O$). All liquid standards were obtained from Sigma Aldrich. Species were detected within the PTRMS as the protonated parent ion, except α-pinene oxide which was detected as $C_{10}H_{17}O^+$ and $C_{10}H_{15}^+$. Liquid standards were diluted in cyclohexane and delivered via a syringe pump. 5 SLPM of zero air flowing orthogonally to the syringe passed over the needle and aspirated the calibrant droplet. The PTRMS measurement line (~0.5 m length, 1/8" ID, 80 ºC) was configured to minimize residence times and VOC partitioning to inlet walls. The zero air flow was held constant while the syringe pump speed was varied to produce a calibration curve for each species. Sensitivities were obtained as a function of humidity across the range of field-measured $H_2O{\cdot}H_3O^+$:H_3O^+ ratios (where H_3O^+ ~ 500 × $H_3{}^{18}O^+$). All humidity-dependent sensitivities were calculated relative to β-pinene, a species calibrated in the field, enabling dynamic calibration corrections based on field conditions. **Figure S2** shows the range of measured sensitivities for monoterpenes, while **Figure S3** summarizes the sensitivities for all calibrated species for a typical humidity level.

S2.2 Formaldehyde calibrations and signal corrections for formulae containing multiple species

Formaldehyde calibrations were performed following the field study by diluting a 4958 ppb standard (certified 19 September 2022) into across relevant humidity (i.e., $H_2O{\cdot}H_3O^+$:H_3O^+) levels. The low ambient water vapor concentrations in this semi-arid ecosystem enabled reliable formaldehyde detection at CH_3O^+. The associated humidity dependence led to a 2-fold sensitivity decrease across the encountered water vapor concentrations (**Fig. S4a**), and this dependence was accounted for during calibration.

Prior work has shown that other VOCs (namely methanol and methyl hydroperoxide; Inomata et al., 2008) can fragment to also produce CH_3O^+ ions. Analysis of our VOC cylinders and liquid standards (**Table S1**) indeed revealed a CH_3O^+ interference from methanol (~0.2:1 CH_3O^+:CH_5O^+) and, weakly, from limonene (~0.05:1 CH_3O^+: $C_{10}H_{17}^+$). Since the raw MT signal at $C_{10}H_{17}^+$ (along with that for methyl hydroperoxide at $CH_5O_2^+$) was very low compared to CH_5O^+, only the methanol correction was applied here.

In general, interference corrections for calibrated species proceeded as described below for formaldehyde:

1. The CH_3O^+ signal including both the analyte of interest (formaldehyde) and a fragment species (methanol), was calibrated for the fragment species (methanol).
2. The concentration difference between the fragment mass (CH_3O^+) and the parent mass for the same species (CH_5O^+) was then calculated to obtain a residual concentration.
3. That residual concentration was converted back to signal units based on the methanol sensitivity.
4. The residual signal was then calibrated for formaldehyde.

The corrected formaldehyde timeseries exhibits a different diel cycle and concentration range than the uncorrected version (**Fig. S4b**). Removal of the fluctuating methanol signal also changed the inferred net formaldehyde flux from primarily upward to bidirectional (**Fig. S4c**). The above procedure was similarly performed for isoprene to correct for $C_5H_9^+$ interference from 232-MBO. The α-pinene oxide contribution to $C_{10}H_{17}O^+$ was likewise removed by attributing the entire $C_{10}H_{15}^+$ signal to that species.

S3 Flux quality control

In addition to the QA/QC described in the main text, flux data were filtered for wind shear and stationarity. Flux periods were discarded if either of the following conditions were met:

1. friction velocity (u_*) < 0.15 m s^{-1}, where

$$u_* = \overline{(w'u'}^2 + \overline{w'v'}^2)^{\frac{1}{4}} \quad \text{(E1)}$$

2. the mean flux for five encompassed sub-periods differed from that for the entire 30-minute window by more than 30% (i.e. stationarity test) (Foken & Wichura, 1996):

$$1 - \frac{\overline{\overline{w'C'}}_{sub-period}}{\overline{\overline{w'C'}}_{full\ period}} > 0.3 \quad \text{(E2)}$$

S4 Spectral corrections

Flux attenuation due to inlet damping, instrument response, and sensor separation was calculated from an empirical model (Horst, 1997) that employs an attenuation time constant, τ_c, also known as the response time. A correction factor is then calculated as:

$$\frac{F_m}{F} = \frac{1}{1+(2\pi n_m \tau_c U/z)^{\alpha}} \quad \text{(E3)}$$

where F_m/F is the ratio of the measured to the unattenuated flux, U is wind speed, z is measurement height, and n_m and α are scaling factors for an unstable boundary layer (taken as 0.085 and 7/8, respectively). The response time can be determined empirically from the ratio of the attenuated scalar normalized cospectra to the unattenuated *w'T'* cospectra and is calculated as the frequency where the attenuated signal is reduced by $1/\sqrt{2}$. For the PTRMS species ΣMT and 232-MBO the resulting τ_c ~ 1 s, requiring a 6% flux correction at the campaign-mean daytime windspeed of 2.1 m s^{-1}, while for ΣSQT and MTO τ_c ~ 5 s, requiring a 25% correction. For the ICIMS species HCOOH τ_c ~ 0.4 s (2.7% correction).

S5 GEOS-Chem land cover updates

The 0.25° × 0.3125° model grid cell containing the MEFO site has heterogenous land cover made up of 6 Community Land Model (CLM) classifications, with 48% of the surface designated as crop cover or bare ground. This is not representative of the 1 x 1 km^2 measurement footprint which primarily consists of ponderosa pine, grass, and shrubs (**Fig S10**). We therefore modified the model land cover and leaf area to simulate biosphere-atmosphere exchange more accurately.

Updates employed Landsat imagery from the United States Geological Survey (USGS) EarthExplorer tool (https://earthexplorer.usgs.gov/). Imagery was obtained encompassing the site and the surrounding land area (300 m in the prevailing wind directions) to capture the highest density portions of the flux footprint. This imagery then underwent k-means clustering-based image segmentation as part of the MATLAB Statistics and Machine Learning Toolbox, with pixels separated into three clusters representing "tree crowns", "tree base and shadows", and grass". The

corresponding pixel fractions then yielded a ponderosa pine fraction of 0.7 and a grass fraction of 0.3, the latter of which we treat in the model as C3 non-arctic grass.

A model LAI of 2.36 m^2 m^{-2} was then obtained by assuming a standard LAI of 3 m^2 m^{-2} for needleleaf evergreen temperate trees (as applied for a MEGAN v2.1 analysis at the same site; Kaser et al., 2013a) and 1 m^2 m^{-2} for grass (a median estimate for temperate 15-25 cm grasses; Byrne et al., 2005). The resulting value is higher than the MODIS-derived ecosystem average (1.4 m^2 m^{-2}) as well as previous estimates for the entire Manitou Experimental Forest (1.2 m^2 m^{-2}; Berkelhammer et al., 2016) but was found to be more appropriate for our site based on a comparisons of our leaf- and canopy-level flux observations.

Basal VOC emissions were obtained by combining MEGAN v3.2 leaf area emission factors (mg compound m^{-2} leaf hr^{-1}) with the fractional ponderosa pine and C3 non-arctic grass coverage scaled by species-specific LAI. The site LAI of 2.36 m^2 m^{-2} was used in the Parameterized Canopy Environment Emission Activity (PCEEA) algorithms (Guenther et al., 2006). The site LAI was also used in the model dry deposition routines with the Olson et al. (2001) "dry evergreen woods" land cover classification.

S6 The effect of mountain-valley flow on morning 232-MBO observations

A mountain-valley flow pattern causes a nighttime south-to-north drainage flow of cold, dense air from higher elevations that leads to stratification at the MEFO site and suppresses vertical mixing. During the day, high-pressure conditions lead to upslope flow from the north, destratification, dynamic instability, and turbulent vertical mixing. The morning transition from mountain- to valley-flow features a unique set of environmental conditions that creates the early flux peak seen in **Fig. 2**. Chemical species with light-dependent leaf-level emissions (e.g., 232-MBO and some MT isomers) are emitted in the pre-transition daylight hours but not yet vertically mixed, so that concentrations build up near the surface. During the subsequent transition, the developing vertical mixing coupled to a large concentration gradient causes a large but short-lived upward flux as the canopy vents. This is illustrated in **Fig. S12**, where the turbulent vertical mixing strength is approximated as the standard deviation in vertical wind (σ_w), and the short-term 232-MBO flux enhancements are seen to coincide with low but increasing σ_w. This behavior was not reported

previously by Kaser et al. (2013a) based on long term 232-MBO flux measurements at this site, which could be due to their use of strict shear stress filters that removed this period of low σ_w and low u_* (~ 0.1-0.15 m/s). Karl et al. (2014) reported a morning build up in 232-MBO concentrations but not flux during a week-long study at this site; the difference could reflect their limited study timeframe or more strict flux filtering.

S7 Rate constant assignments for MT, SQT, and species with unknown k_{O3}

For ΣMT we applied the α-pinene rate coefficents (k_{OH} = 5.2 x 10^{-11} cm^3 $molecules^{-1}$ s^{-1} and k_{O3} = 8.7 x 10^{-17} cm^3 $molecule^{-1}$ s^{-1} at 298 K) (Atkinson et al., 1990; Atkinson & Arey, 2003) since those were the median values across observed MT. For ΣSQT we employed a k_{OH} that represents the average across five isomers (α-cedrene; α-copaene; β-caryophyllene; α-humulene; longifolene; 1.4 x 10^{-10} cm^3 $molecules^{-1}$ s^{-1} at 298 K) (Atkinson & Arey, 2003) and the β-caryophyllene k_{O3} value (1.1 x 10^{-14} cm^3 $molecule^{-1}$ s^{-1} at 298 K) (Richters et al., 2015). Understory measurements during our study pointed to important contributions from β-farnesene, sesquisabinene, and β-sesquiphellandrene, of which only β-farnesene has a published ozone rate coefficient (7 x 10^{-16} cm^3 $molecule^{-1}$ s^{-1} at 298 K) (Kim et al., 2011). Since the other two quantified SQTs contain rings and endo- and exocylic double bonds we assume the collective rate constant is closer to that for β-caryophyllene (1.1 x 10^{-14} cm^3 $molecule^{-1}$ s^{-1} at 298 K). Furthermore, prior GC measurements at this site found β-caryophyllene to be the largest contributor to ambient ΣSQT concentrations (Chan et al., 2016), while other leaf level measurements for ponderosa pine have identified β-caryophyllene as a contributing isomer (Helmig et al., 2017). For consistency, the same ΣMT and ΣSQT rate coefficients were applied to both observations and model.

Molecules with known formulae but unknown rate coefficients for reaction with ozone were assigned k_{O3} values based on their DBE, with k_{O3} = 0, 8.6 × 10^{-18}, 8.1 × 10^{-17}, and 1.5 × 10^{-16} cm^3 $molecule^{-1}$ s^{-1} for DBE = 0, 1, 2, and ≥3. These values were obtained as the median in each case across observed species with known k_{O3}.

We estimate the uncertainties in k_{OH} and k_{O3} for unknown species at a factor of 10 by applying the same methodology to all measured species with known structure and k_{Y+VOC}. The resulting upper

limits for each unknown VOC are capped at $k_{OH} = 1.39 \times 10^{-10}$ (the value for ΣSQT) and $k_{O3} = 1.9 \times 10^{-6}$ (the value for butene).

Supplementary Tables

Species name	Formula	Concentration (ppb)
Acetaldehyde	CH_3CHO	1028
Methanol	CH_3OH	4969
Acetonitrile	CH_3CN	1008
Acetone	CH_3COCH_3	2439
Isoprene	C_5H_8	2477
Methyl ethyl ketone	C_4H_8O	1049
Hydroxyacetone	$C_3H_6O_2$	1280
Benzene	C_6H_6	1047
Toluene	C_7H_8	1042
m-Xylene	C_8H_{10}	1018
1,3,5-Trimethylbenzene	C_9H_{12}	950
1,2,4,5-Tetramethylbenzene	$C_{10}H_{14}$	990
Propene	C_3H_6	1001
Furan	C_4H_4O	1037
DMS	C_2H_6S	1065
Methacrolein	C_4H_6O	1047
2-Methyl-3-Buten-2-ol	$C_5H_{10}O$	1040
3-Hexanone	$C_6H_{12}O$	1003
β-pinene	$C_{10}H_{16}$	1009
Propyne	C_3H_4	970
1-Butene	C_4H_8	982
Ethanol	C_2H_6O	1032
Methyl Vinyl Ketone	C_4H_6O	979
3-Methyl Furan	C_5H_6O	973
3-Pentanone	$C_5H_{10}O$	1025
Ethyl Benzene	C_8H_{10}	991
α-pinene	$C_{10}H_{16}$	997

Table S1: Species and concentrations contained in VOC cylinders used for in-field PTRMS calibration. All species certified 5 November 2021 with an uncertainty of +/- 5%.

Reaction[a]	k (cm^3 molecule^{-1} s^{-1})[b]
MBO + OH → 0.52ACET + 0.35CH_2O + 0.50ACTA	8.1×10^{-12}*exp(610/T)
MBO + NO_3 → 0.68ACET + 0.13ITHN	4.6×10^{-14}*exp(-400/T)
MBO + O_3 → 0.08ACET + 0.47CH_2O	1.0×10^{-17}
RCOOH + OH → OTHRO2	1.2×10^{-12}
SESQ + OH → KO_2 + products	1.97×10^{-10}
SESQ + O_3 → KO_2 + OH + products	1.2×10^{-14}
SESQ + NO_3 → INDIOL	1.90×10^{-11}

Table S2: Additions to the GEOS-Chem chemical mechanism.
[a] molar yields for MBO reactions taken from Fantechi et al. (1998) and Ferronato et al. (1998)
[b] all rate constants taken from MCM v3.3.1 (Saunders et al., 2003)

Species	H^* (M atm^{-1})	f_0
RCOOH	5×10^{-3}	1

Table S3: Additions to the GEOS-Chem dry deposition scheme. Henry's law constants are taken from Sander (2015) and reactivity factors for oxygenated VOCs are set to 1 following Karl et. al (2010)

	Upward VOC-Carbon	Downward VOC-Carbon	Upward OH Reactivity	Downward OH Reactivity	Upward O_3 Reactivity	Downward O_3 Reactivity
1.	$C_5H_{10}O$	$C_3H_6O_2$	$C_5H_{10}O$	CH_2O	$C_{15}H_{24}$	CHON
2.	$C_{10}H_{16}$	CH_2O	$C_{10}H_{16}$	*$C_5H_{10}O_3$*	$C_{10}H_{16}$	*$C_3H_3O_3$*
3.	C_2H_6O	*$C_5H_{10}O_3$*	C_5H_8	$C_3H_6O_2$	$C_5H_{10}O$	*$C_4H_6O_3$*
4.	CH_4O	*$C_4H_8O_3$*	$C_{15}H_{24}$	*$C_4H_6O_3$*	C_4H_8	*$C_4H_6O_4$*
5.	C_5H_8	*$C_4H_6O_3$*	C_2H_4O	*$C_5H_9NO_4$*	C_5H_8	*$C_3H_4O_3$*
6.	$C_3H_6O_2$	*$C_5H_9NO_4$*	CH_2O	*$C_3H_3O_3$*	C_3H_4O	*$C_4H_4O_3$*
7.	$C_{15}H_{24}$	*$C_3H_3O_3$*	C_2H_6O	*$C_4H_6O_4$*	C_6H_6	*$C_5H_9NO_4$*
8.	C_3H_6O	$C_2H_4O_2$	$C_3H_6O_2$	*$C_5H_9NO_5$*	C_5H_6O	*$C_4H_7NO_5$*
9.	C_2H_4O	*$C_3H_6O_3$*	$C_4H_8O_2$	*$C_3H_6O_3$*	C_4H_4	*$C_2H_3NO_2$*
10.	CH_2O	*$C_4H_6O_4$*	C_4H_6O	*$C_4H_7NO_5$*	C_8H_8	*$C_5H_9NO_5$*

Table S4: Top ten contributors to the observed upward and downward fluxes. Species detected with the ICIMS are in *italics*; others were detected by PTRMS. PTRMS compounds were detected as protonated species (MH^+) and ICIMS species were detected as iodide adducts (IM^-)

Species	Formula	Full name
ACET	C_3H_6O	Acetone
ACTA	$C_2H_4O_2$	Acetic acid
ALD2	CH_3CHO	Acetaldehyde
C2H6	C_2H_6	Ethane
CH2O	CH_2O	Formaldehyde
EOH	C_2H_6O	Ethanol
GLYC	$C_2H_4O_2$	Glycoaldehyde
HCOOH	HCOOH	Formic acid
HMHP	CH_4O_3	Hydroxymethyl hydroperoxide
HMML	$C_4H_6O_3$	hydroxymethyl-methyl-a-lactone
ICHE	$C_5H_8O_3$	Isoprene hydroxy-carbonyl-epoxides
IDHDP	$C_5H_{12}O_6$	Isoprene dihydroxy dihydroperoxide
IDN	$C_5H_8N_2O_6$	Lumped isoprene dinitrates
IEPOX	$C_5H_{10}O_3$	Isoprene epoxide
IEPOXA	$C_4H_{10}O_3$	trans-Beta isoprene epoxydiol
IEPOXB	$C_4H_{10}O_3$	cis-Beta isoprene epoxydiol
ISOP	C_5H_8	Isoprene
ISOPNB	$C_5H_9NO_4$	Isoprene nitrate Beta
ISOPND	$C_5H_9NO_4$	Isoprene nitrate Delta
ITHN	$C_5H_{11}NO_7$	Lumped isoprene tetrafunctional hydroxynitrates
INDIOL	--	Generic aerosol-phase organonitrate hydrolysis product
KO_2	$C_4H_5O_3$	Peroxy radical from >3 ketones
MACR	C_4H_6O	Methacrolein
MAP	$C_2H_4O_3$	Peroxyacetic acid
MBOX	$C_5H_{10}O$	2-methyl-3-buten-2-ol
MOH	CH_3OH	Methanol
MONITS	$C_{10}H_{17}NO_4$	Saturated 1st gen monoterpene organic nitrate
MP	CH_3OOH	Methyl hydro peroxide
MTPA	$C_{10}H_{16}$	α-pinene, β-pinene, sabinene, carene
MVK	C_4H_6O	Methyl vinyl ketone
MVKPC	$C_4H_6O_4$	MVK hydroperoxy-carbonyl
OTHRO2	$C_2H_5O_2$	Other C2 RO_2 not from C_2H_6 oxidation
PAN	$C_2H_3NO_5$	Peroxyacetyl nitrate
PIP	$C_{10}H_{18}O_3$	Peroxide from MTPA
PPN	$C_3H_5NO_5$	Lumped peroxypropionyl nitrate
RCOOH	$C_3H_6O_2$	>C2 organic acids
SQT	$C_{15}H_{24}$	Sesquiterpenes
TSOG	--	Lumped semivolatile gas products of monoterpene + sesquiterpene oxidation
XYLE	C_8H_{10}	Xylene

Table S5: GEOS-Chem species names and formulae used in this analysis.

Supplementary Figures

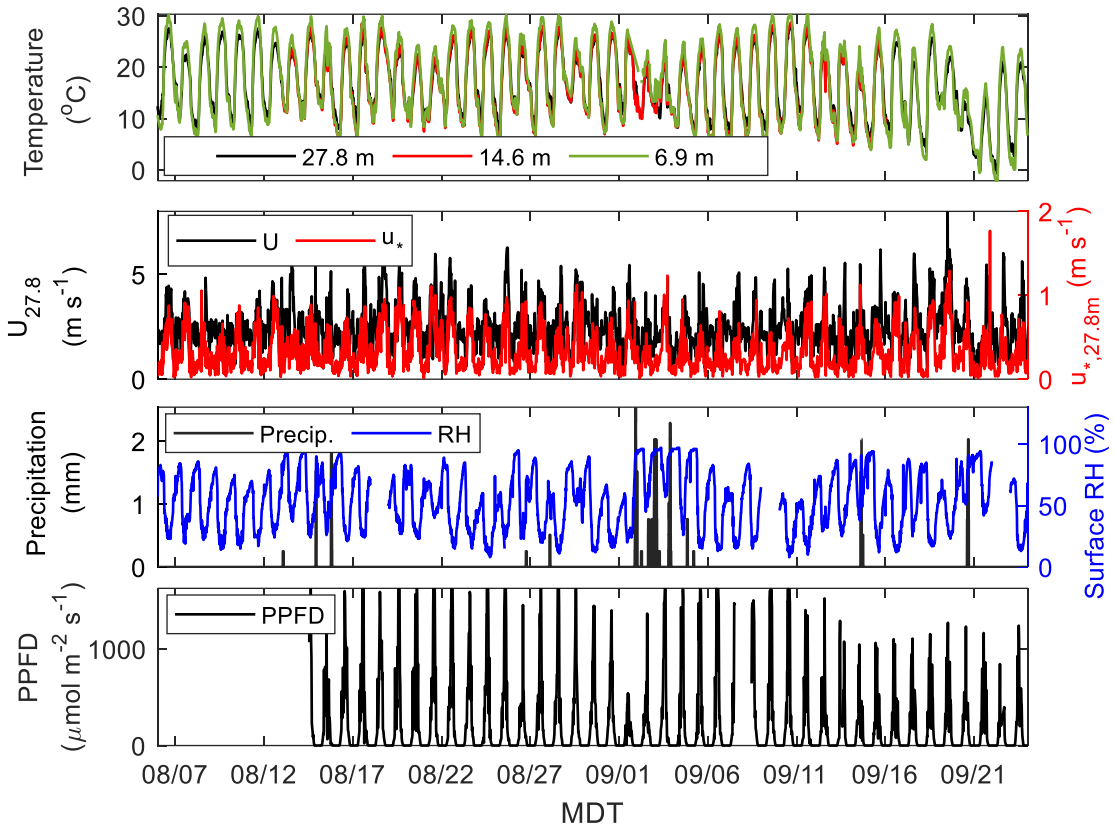

Figure S1: Meteorology during the FluCS 2021 study: a) sonic temperature at three heights, b) horizontal wind (U) and friction velocity (u_*) at 27.8 m, c) precipitation and relative humidity, d) surface photosynthetically active radiation (PAR).

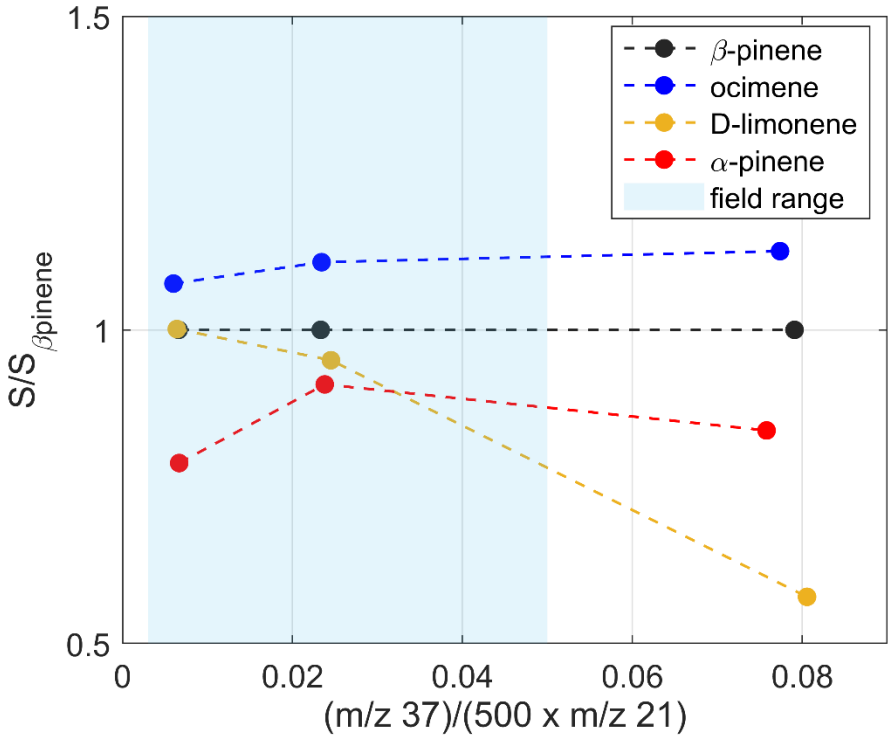

Figure S2: Sensitivities (S) for monoterpenes observed at MEFO relative to β-pinene (circles) over a range of PTRMS water concentrations. Water concentrations are calculated as the ratio of the protonated water dimer (m/z 37; $H_2OH_3O^+$) to the protonated water isotope scaled by abundance (500 × m/z 21; $H_3{}^{18}O^+$). Also indicated is the range of water concentration encountered during FluCS 2021 (blue shaded region).

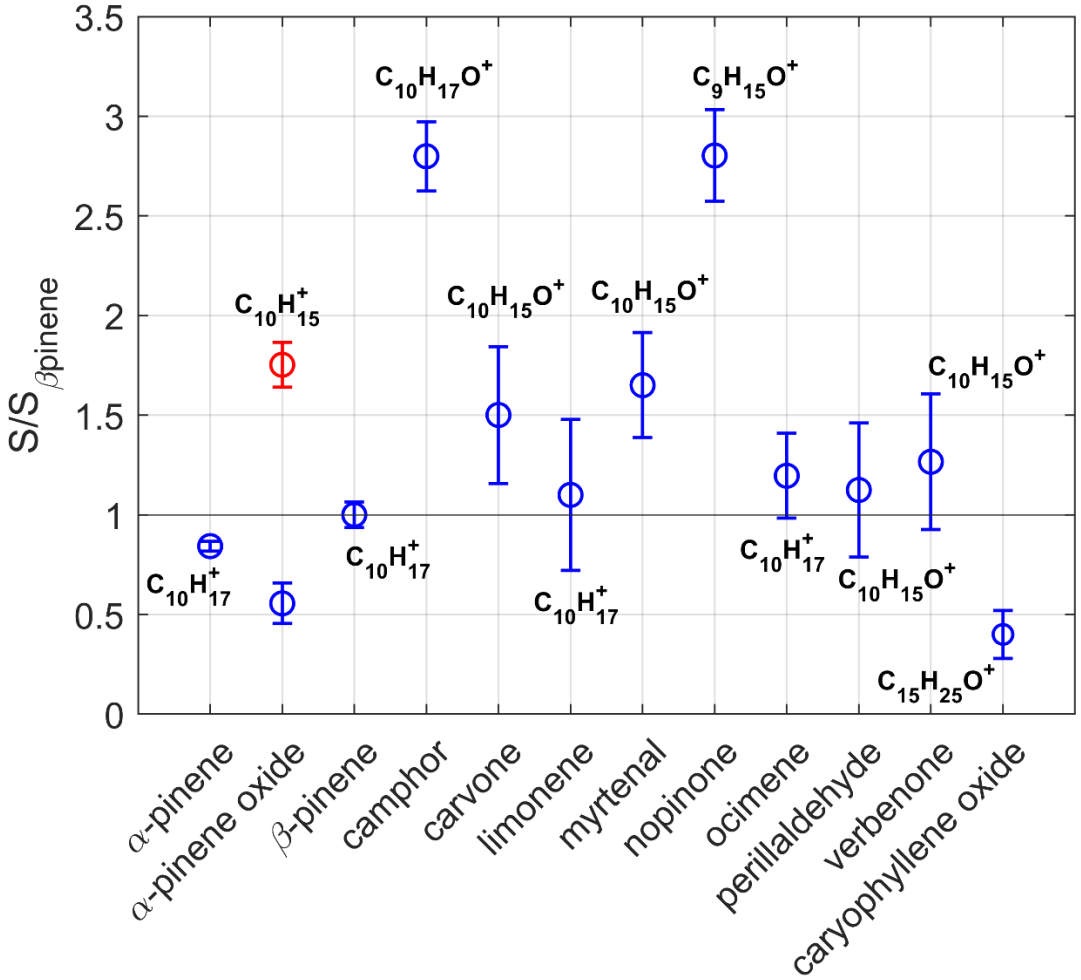

Figure S3: Example compound sensitivities (S) relative to that for β-pinene ($S_{\beta\text{-pinene}}$) measured in-laboratory via liquid calibration. All sensitivities are plotted for the median water concentration for the study. All masses were calibrated at the parent ion (blue circles), except α-pinene oxide (red circle) which was calibrated at both the parent ion and fragment.

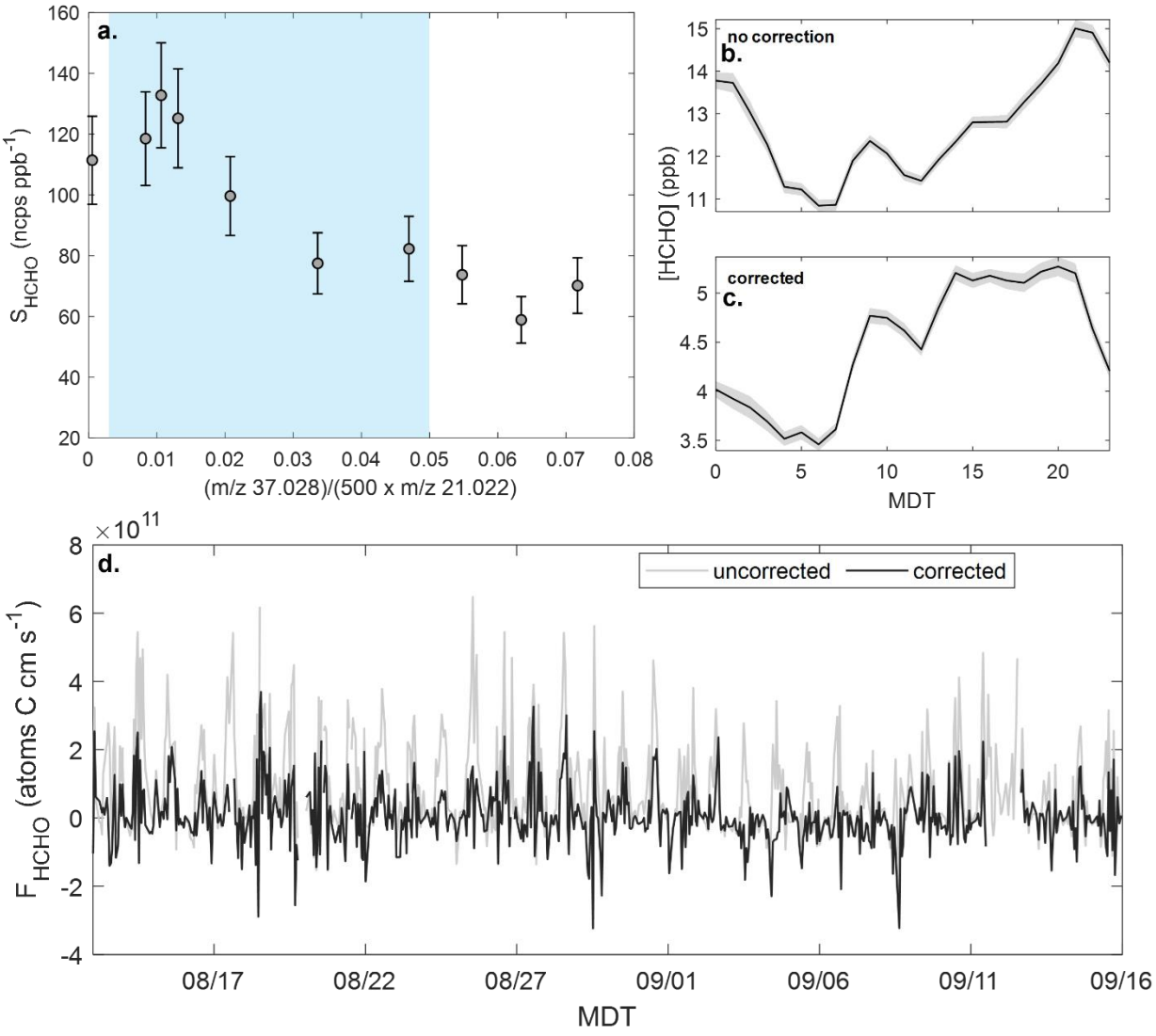

Figure S4: Summary of HCHO calibration and correction results. a) Humidity dependence of the HCHO sensitivity (S_{HCHO}) under different water concentrations. Calibrated HCHO concentrations (b) without correcting for the methanol interference, and (c) after correction. (d) Calibrated HCHO flux before and after methanol correction.

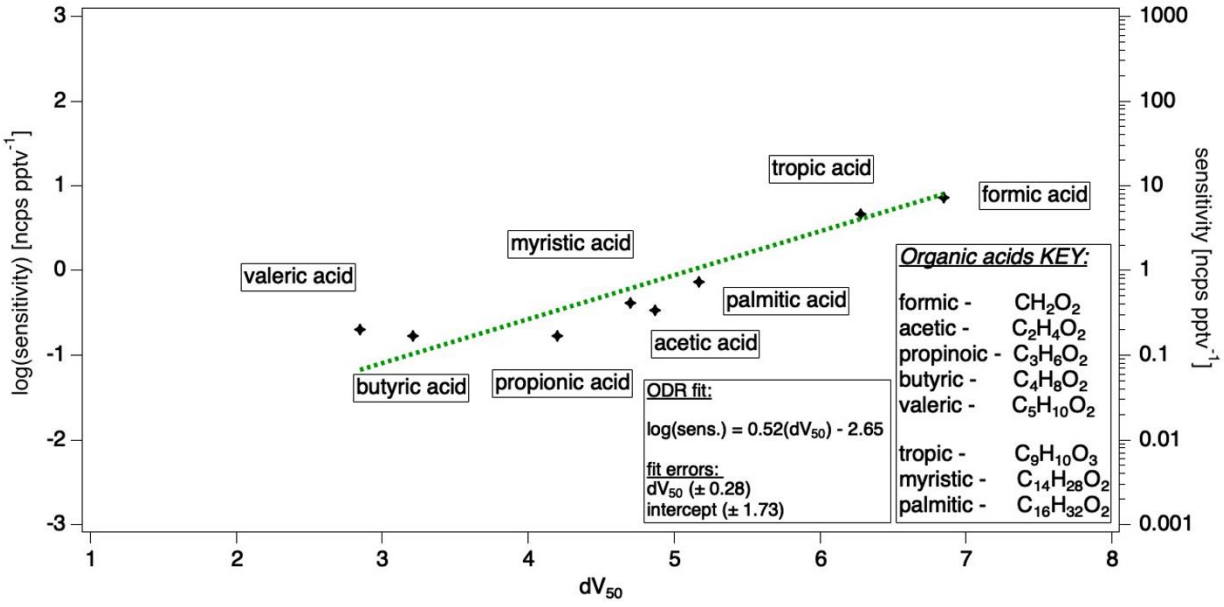

Figure S5: Log-linear dependence of ICIMS sensitivity on dV_{50}. The inset ODR fit was used for calculating ICIMS sensitivity.

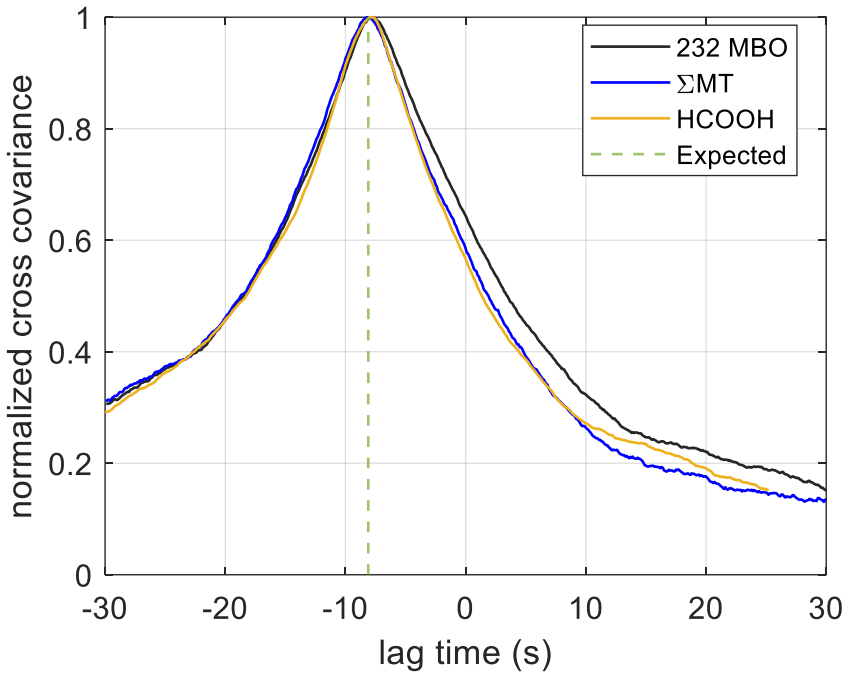

Figure S6: Normalized daytime averaged cross-covariance for 232-MBO and ΣMT (measured by PTRMS) and HCOOH (measured by ICIMS). The dashed line indicates the expected lag time based on the calculated air residence within the flux sampling inlet.

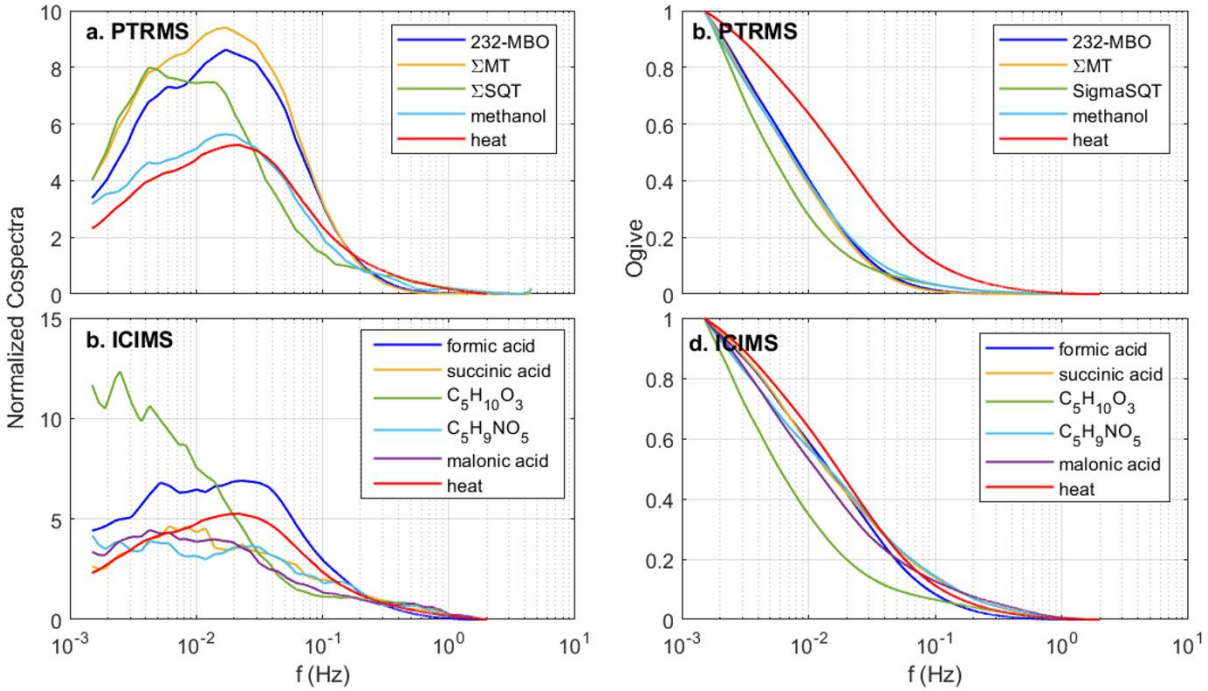

Figure S7: Frequency-normalized cospectra and ogives for high-signal species measured by PTRMS (a + b) and ICIMS (c + d). Cospectra and ogives for the unattenuated sensible heat flux (red lines) are included for reference.

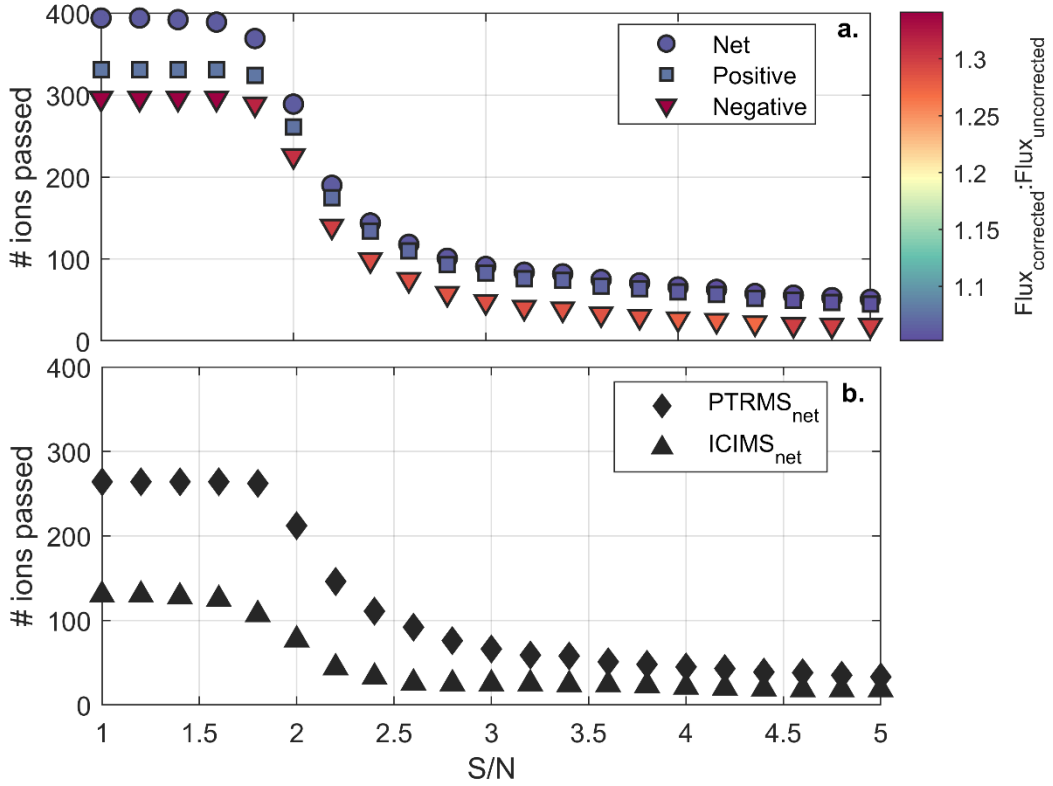

Figure S8: Ion filters based on signal to noise (S/N) evaluation. a) The number of ions with corresponding S/N values for the net, upward, and downward VOC-C fluxes. b) The number of ions with corresponding S/N values for the net PTRMS ICIMS fluxes. The weighted spectral correction factor relative to the uncorrected flux is indicated by the colorbar.

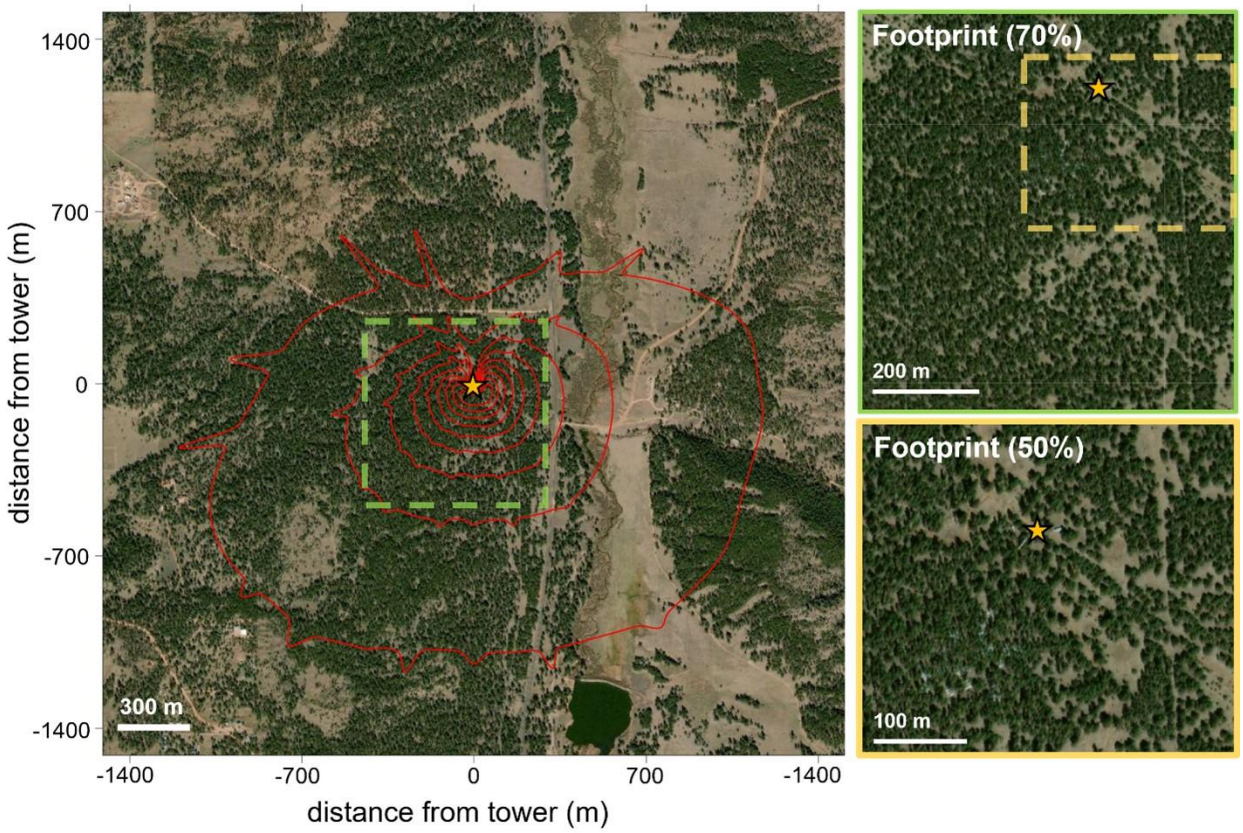

Figure S9: Daytime flux footprint contours (up to 80%) overlaid on geostationary imagery. Included are enhanced images within the 80% and 50% contours, the latter of which contains the highest sampling probability and is used for calculating in-footprint plant functional type contributions.

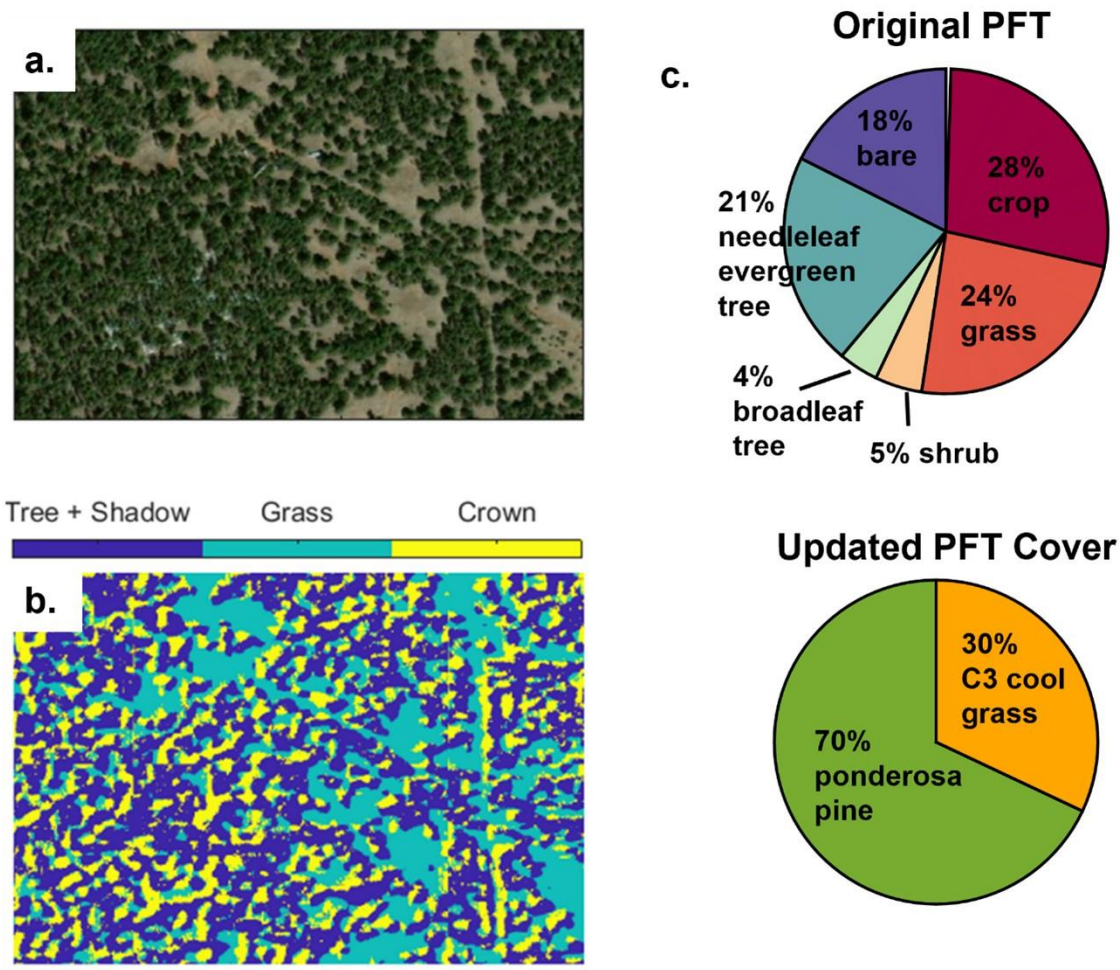

Figure S10: Calculation of plant functional type (PFT) contributions from geostationary imagery. Land cover imagery within the 50% flux footprint (a) undergoes k-means clustering (b) to separate pixels into three groups: "tree and shadow" (dark blue), "grass" (teal), and "tree crown" (yellow). The clusters are separated into ponderosa pine and C3 grass, and the results (c) used to update the default GEOS-Chem land cover within the corresponding model grid cell.

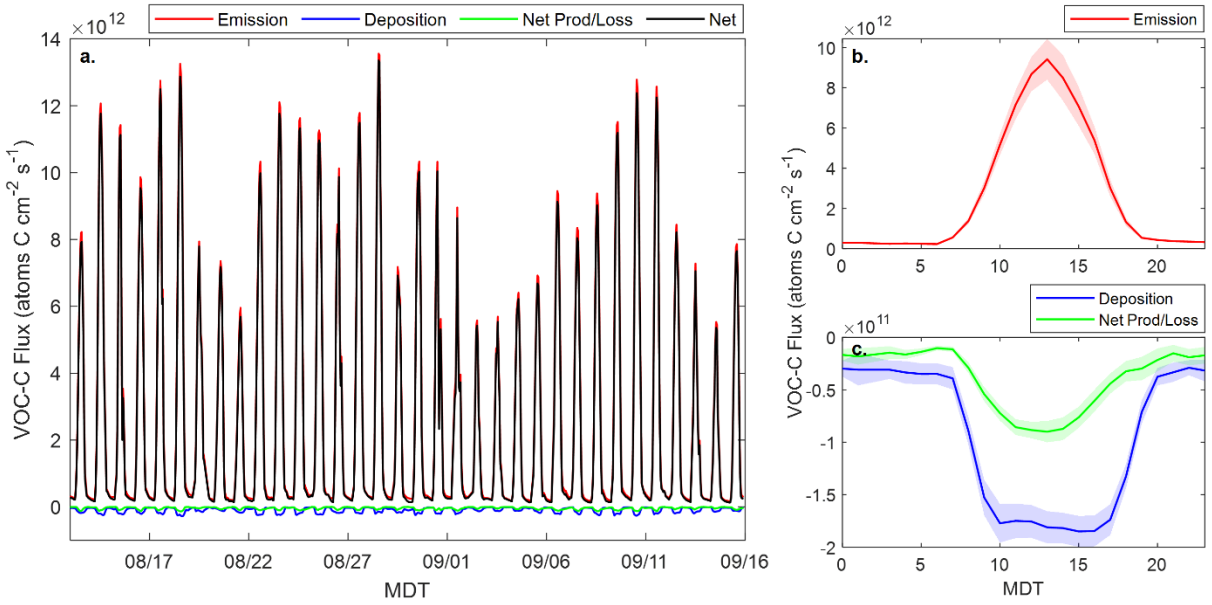

Figure S11: a) Model-simulated fluxes due to emissions (red), deposition (blue), and chemistry (green) along with the resulting net flux (black). The corresponding diel profiles (b, c) show that the GEOS-Chem emission fluxes are ~50× larger than the downward fluxes, while deposition and chemistry are closer in magnitude.

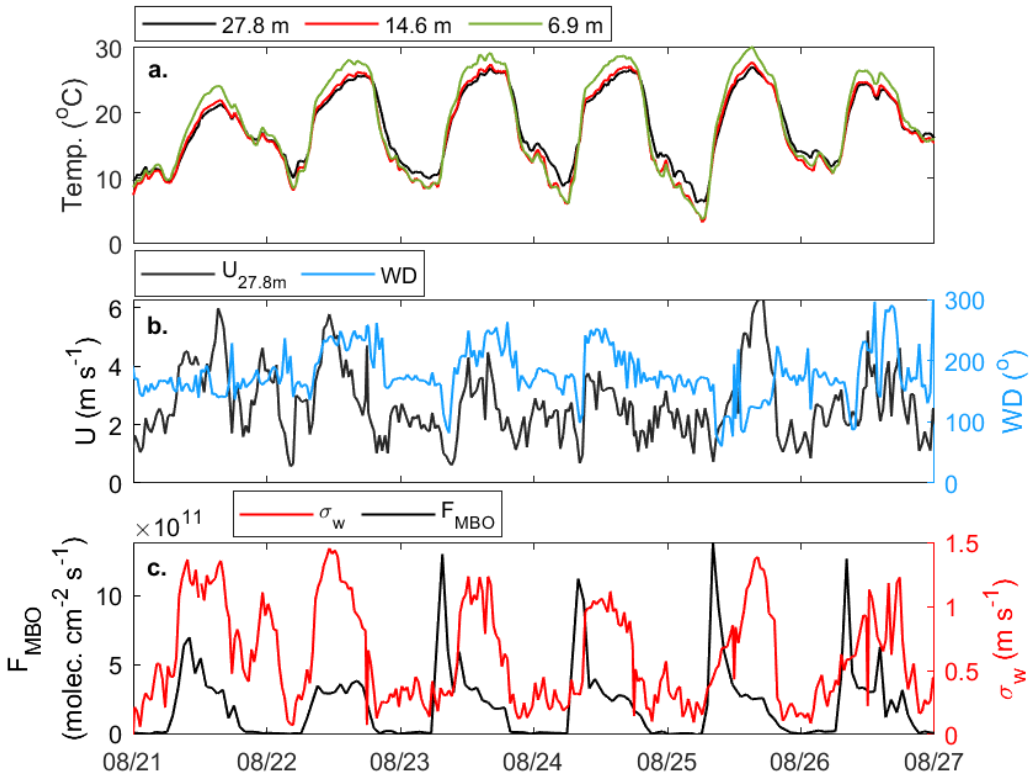

Figure S12: Example timeseries showing the coupling between low but developing morning-time vertical mixing and 232-MBO flux enhancements. A changing temperature gradient (a) is accompanied by a drop in windspeed and shifting wind direction (b). The same transition period also witnesses changes in the standard deviation of vertical wind (σ_w) and enhanced 232-MBO flux.

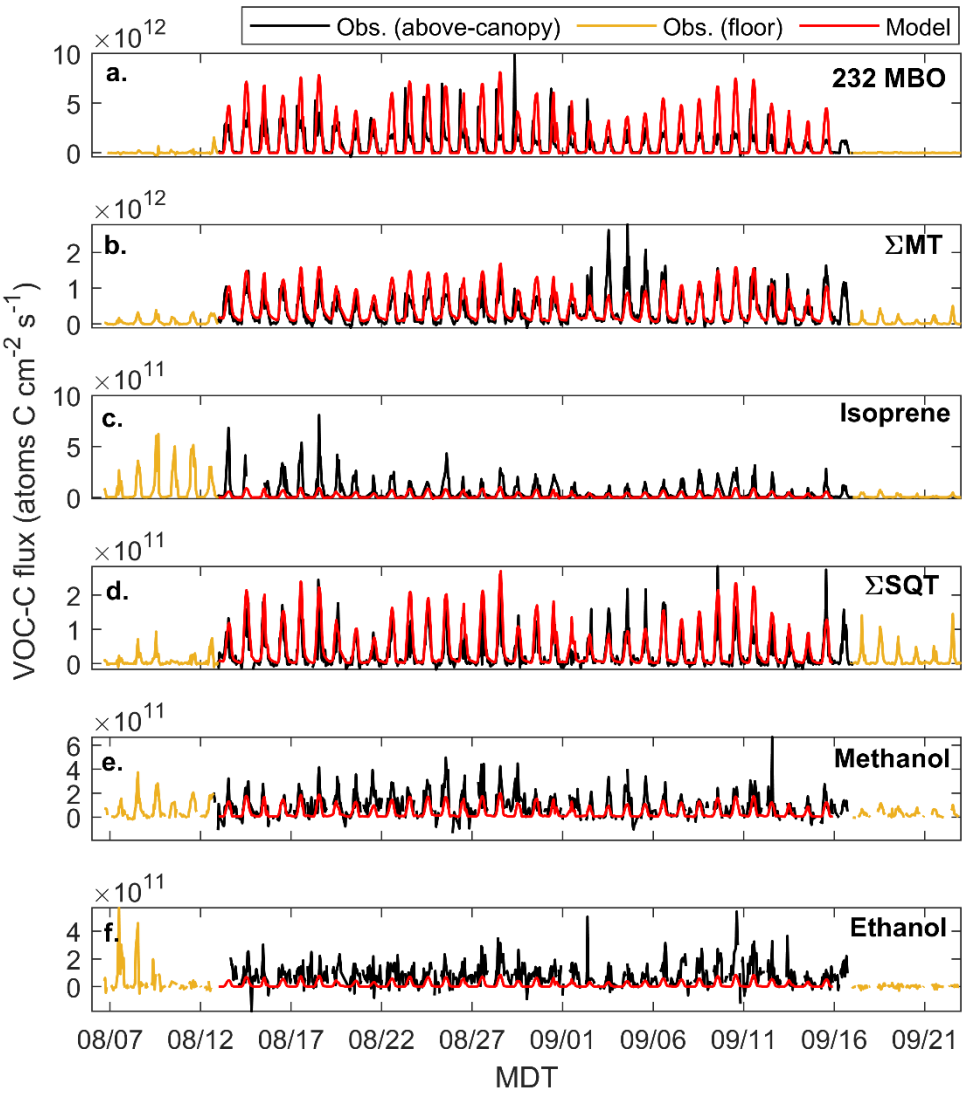

Figure S13: Above-canopy (27.8 m, black) and forest floor (1.9 m, yellow) VOC-C flux measurements for a) 232-MBO, b) ΣMT, c) isoprene, d) ΣSQT, e) methanol, and f) ethanol. The corresponding above-canopy model predictions are shown in red.

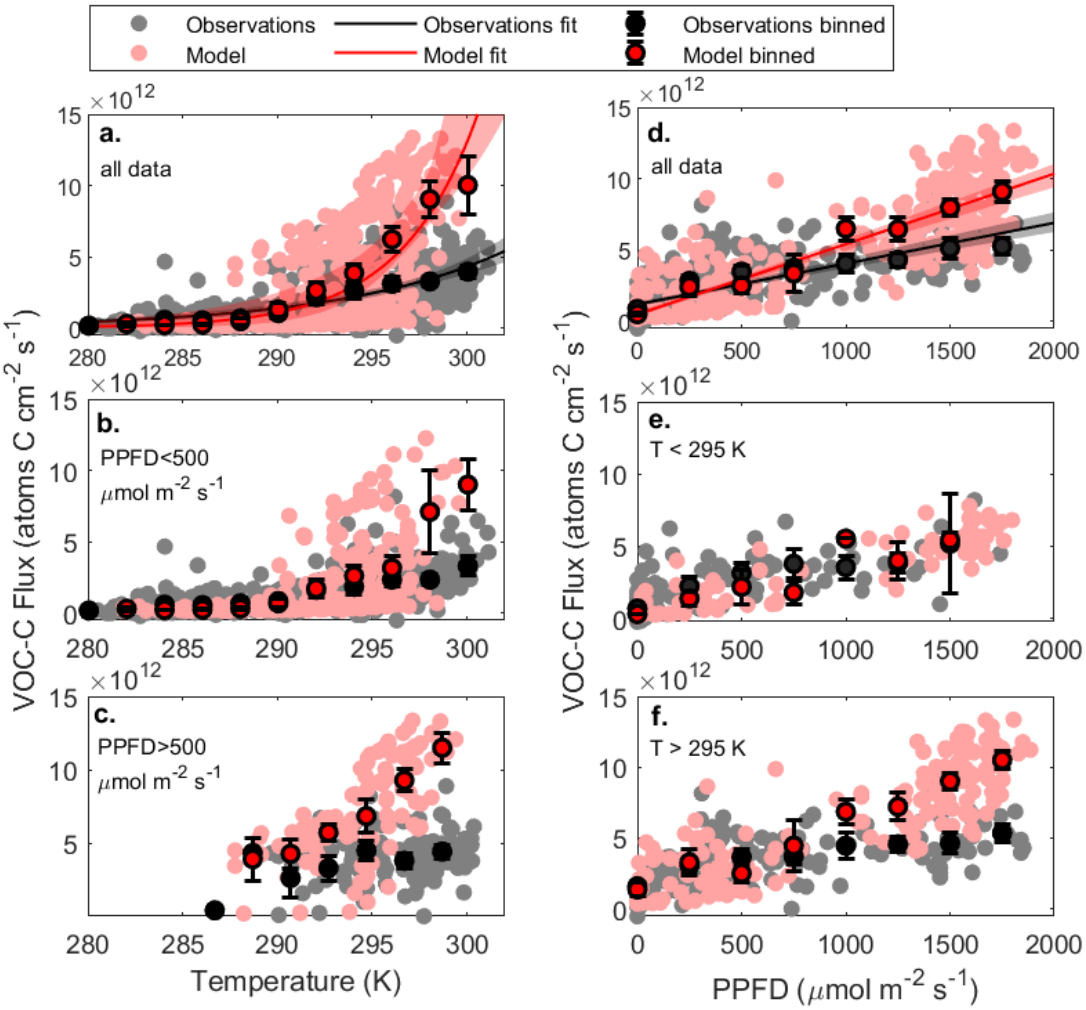

Figure S14: Temperature and light sensitivity of the observed (black) and modeled (red) VOC-C fluxes. The flux-temperature dependence is plotted for a) all data, b) PPFD > 500 μmol m^{-2} s^{-1}, and c) PPFD < 500 μmol m^{-2} s^{-1}. The flux-light dependence is plotted for d) all data, e) T < 295 K, and f) T > 295 K. Temperature fits follow the form $y = a\exp^{b(x-297)}$) with coefficients and bootstrapped 95% confidence intervals presented in the main text. Fits for PPFD are linear, $y = cx + d$, with fits, 95% bootstrapped confidence intervals, and correlation coefficients for the full data ensemble of: $c_{obs} = 2.9\times10^{9}$ [2.6×10^{9}, 3.1×10^{9}], $c_{mod} = 4.9\times10^{9}$ [4.7×10^{9}, 5.2×10^{9}], $d_{obs} = 1.2\times10^{12}$ [1.0×10^{11}, 1.3×10^{12}], $d_{mod} = 4.6\times10^{11}$ [3.6×10^{11}, 6.1×10^{11}], $r^2_{obs} = 0.56$, $r^2_{mod} = 0.81$.

537

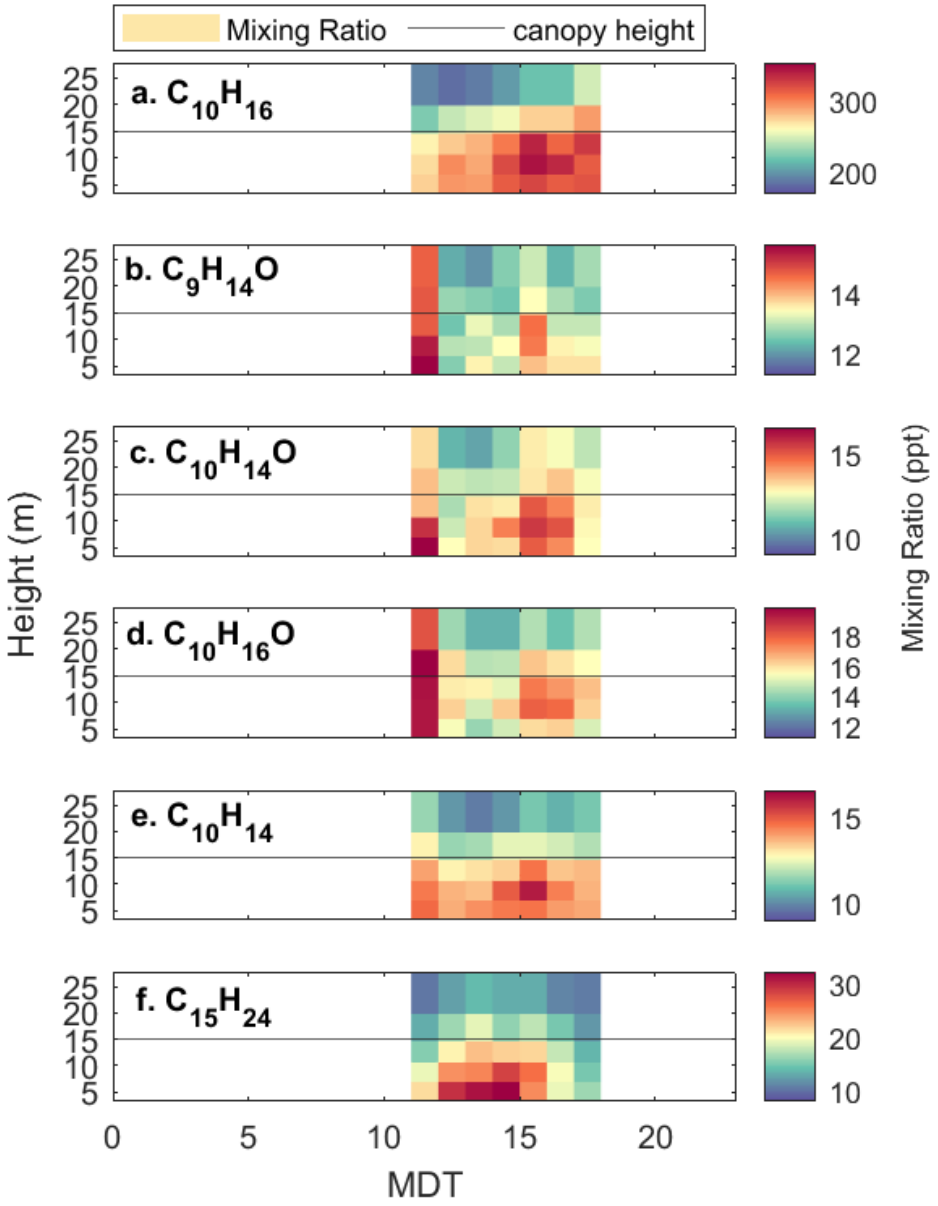

538
539 **Figure S15**: Diel concentration gradients for (a) ΣMT, (b-e) MT oxides, and (f) ΣSQT averaged over the
540 entire study. Horizontal line indicates the canopy height within the flux footprint.
541

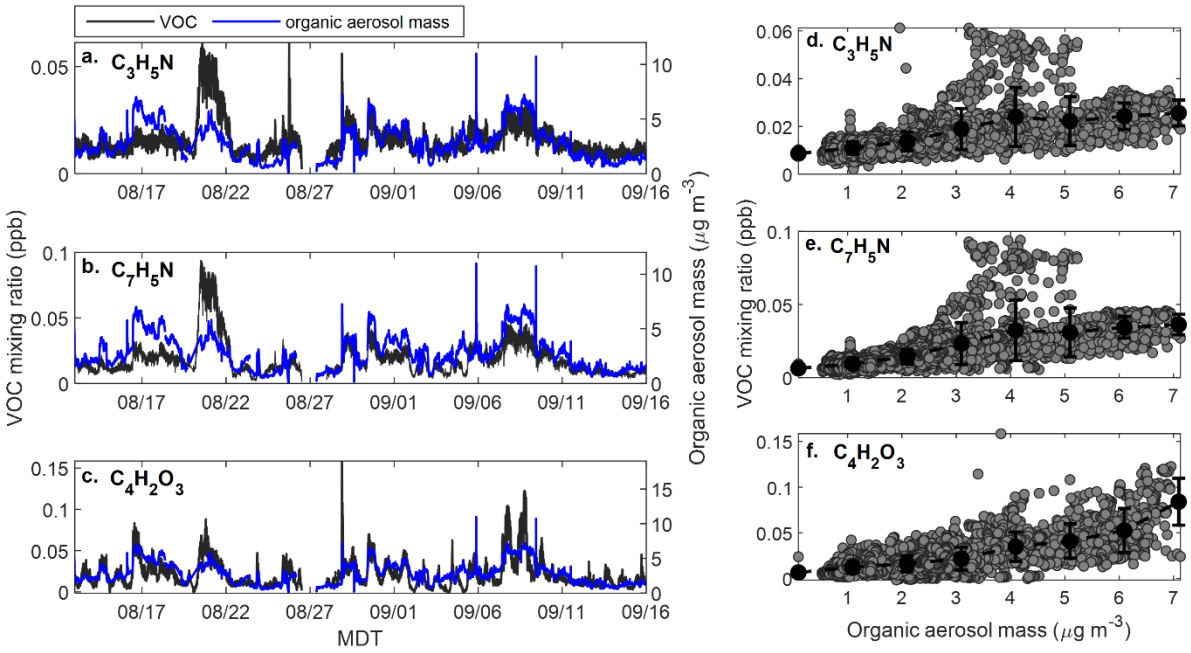

Figure S16: Biomass burning influence during the study as diagnosed with PTRMS-derived VOC tracers (black) and AMS-derived organic aerosol mass (OA, blue line). Data are plotted separately for a) propanenitrile, b) benzonitrile, and c) maleic anhydride. The corresponding regressions (d-f) show a strong maleic anhydride:OA correlation, while the nitriles exhibit periods where they diverge from OA, indicating a change in fire source or aging.

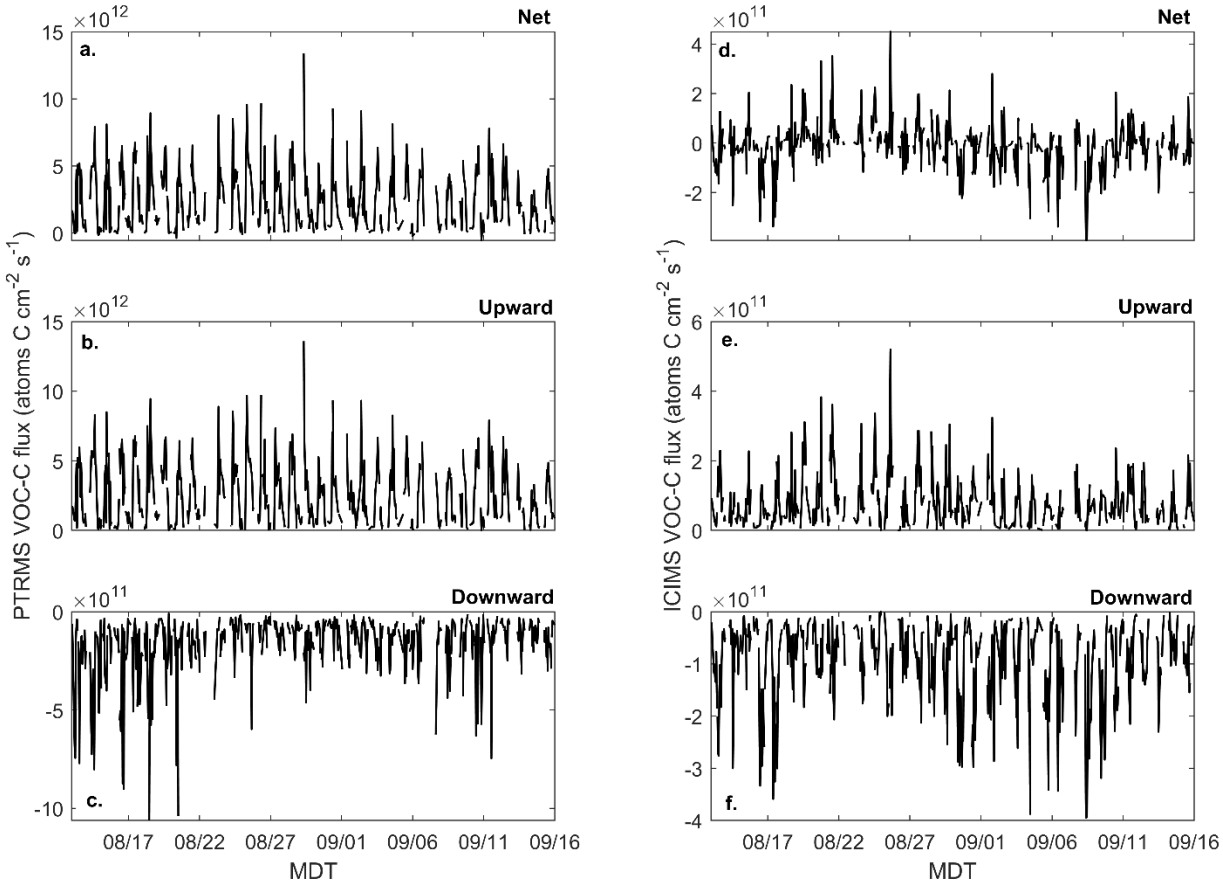

Figure S17: Total net (a + b), upward (b + c), and downward (e + f) VOC-C fluxes as measured by PTRMS and ICIMS.